Beyond Solvent Exclusion: i-Motif Detecting Capability and an Alternative DNA Light Switching Mechanism in a Ruthenium(II) Polypyridyl Complex

Philip Spence[1], John Fielden[2]*, Zoë. A. E. Waller[1]*

[1]School of Pharmacy, University of East Anglia, Norwich, NR4 7TJ, UK

[2]School of Chemistry, University of East Anglia, Norwich, NR4 7TJ, UK

ABSTRACT: Cytosine-rich DNA can fold into secondary structures known as i-motifs. Mounting experimental evidence suggests that these non-canonical nucleic acid structures form *in vivo* and play biological roles. However, to date, there are no optical probes able to identify i-motif in the presence of other types of DNA. Herein, we report for the first time the interactions between the three isomers of $[Ru(bqp)_2]^{2+}$ with i-motif, G-quadruplex and double helical DNA. Each isomer has vastly different light switching properties: **mer** is "on", **trans** is "off" and **cis** switches from "off" to "on" in the presence of all types of DNA. Using emission lifetime measurements, we show the potential of **cis** to light up and identify i-motif, even when other DNA structures are present using a sequence from the promoter region of death associated protein (DAP). Moreover, separated **cis** enantiomers revealed **Λ-cis** to have a preference for i-motif whereas **Δ-cis** has a preference for double helical DNA. Finally, we propose a previously unreported light switching mechanism that originates from steric compression and electronic effects in a tight binding site, as opposed to solvent exclusion. Our work suggests that many published non-emissive Ru complexes could potentially switch-on in the presence biological targets with suitable binding sites, opening up a plethora of opportunity in the detection of biological molecules.

INTRODUCTION

Cytosine rich DNA sequences are able to form i-motifs, four-stranded secondary structures comprised of parallel-stranded DNA duplexes zipped together in an antiparallel orientation by intercalated, cytosine–cytosine$^+$ base pairs.[1,2] i-Motifs are prevalent in genomic DNA[3] and have been shown to play key roles in gene expression.[4,5] With the recent discovery that i-motif DNA forms in human cells,[6] we now know of many secondary structures that DNA can adopt *in vivo*[7] and the need for structural probes is greater than ever. To date, there are no optical probes which are able to identify i-motif in the presence of other types of DNA.

Ruthenium(II) polypyridyl complexes have many advantages over organic dyes as potential *in vivo* fluorescent probes.[8] They possess excellent photophysical properties with intense triplet metal-to-ligand charge transfer (MLCT) bands in the visible region,[9] long emission lifetimes,[10] and good cellular uptake.[11,12] In 1990, Barton and co-workers showed that $[Ru(bpy)_2(dppz)]^{2+}$ (bpy = 2,2′-bipyridine, dppz = dipyrido[3,2-a:2′,3′-c]phenazine) works as a "molecular light switch" in the presence of DNA[13] and since then, many other dppz-based complexes have been synthesized to discover new DNA secondary structure specific light switches.[14] The light-switching effect in dppz complexes originates from the existence of emissive and non-emissive MLCT excited states. Rapid conversion to the non-emissive state is favored by hydrogen bonding to solvent (e.g. water), and solvent exclusion by DNA results in an increased

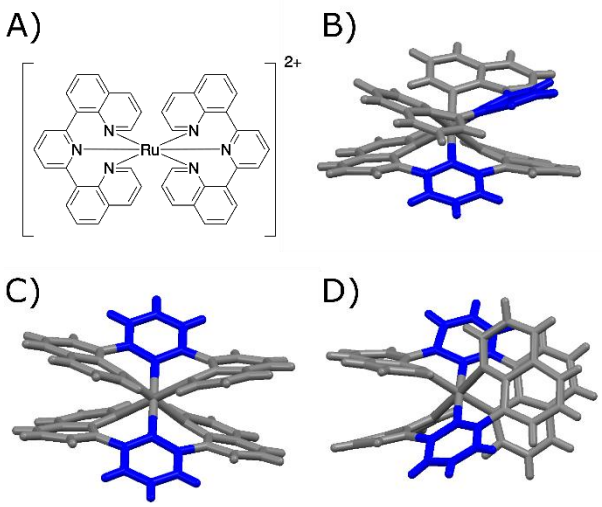

Figure 1 – A) Structure of $[Ru(bqp)_2]^{2+}$. Crystal structures of B) **cis**, C) **trans**, and D) **mer**, with central pyridines colored blue.

quantum yield.[15] Other similar ruthenium-based compounds also contain hydrogen-bonding groups and exhibit similar light switching properties.[16-20] For example, work by Thomas and co-workers has previously described dinuclear ruthenium(II) complexes including those based on the ditopic ligands tetrapyrido[3,2-a:2′,3′-c:3″,2″-h:2″,3″-j] phenazine (tppz). These complexes were found to have a preference for G-quadruplex DNA, and G-quadruplex binding was found to result in a "light-switch" effect, where

emission is blue-shifted and considerably more enhanced relative to duplex binding.[21] This not only enabled detection of G-quadruplex DNA but the complexes were later used as the first 2-photon phosphorescent lifetime imaging microscopy imaging probes for nuclear DNA in cells.[22]

Recently, the complexes $[Ru(phen)_2(dppz)]^{2+}$ and $[Ru(bpy)_2(dppz)]^{2+}$ have been reported to bind i-motif[23,24] and G-quadruplex DNA. The compounds show preference for G-quadruplex binding, derived from end-stacking of the dppz ligand with the G-quartets of the G-quadruplex structure.[25] Since then, the enantiomers Λ- and Δ-$[Ru(L)_2(dppz)]^{2+}$ (where L = bpy or phen) have both been investigated for their interaction with i-motif DNA, using sequences with various loop lengths.[26] This work indicated the emissive properties were driven by the dppz ligands intercalating into the loops, the hypervariable part of i-motif structure which varies between different sequences. The inability of the dppz family of ligands to target the core of the i-motif, and the variability in emission with varying loop lengths, puts limitations on their utility in general identification of i-motif forming sequences. It is necessary to explore other types of probes for studying i-motif.

Motivated by this need, we are exploring the interaction of ruthenium complexes of 2,6-bi(quinolin-8-yl)pyridine (bqp) with i-motif and other forms of DNA. The bqp ligand and its ruthenium complexes (Figure 1) were first developed by Hammerström and co-workers,[27] to provide Ru terpyridine analogues with long ^{3}MLCT emission lifetimes. Consequently, *mer*-$[Ru(bqp)_2]^{2+}$ (**mer**) and derivatives have been well studied for their photophysical properties.[28,29] However, bqp also forms facial isomers: *cis,fac*-$[Ru(bqp)_2]^{2+}$ (**cis**) and *trans,fac*-$[Ru(bqp)_2]^{2+}$ (**trans**).[30] The photophysical properties of these isomers have not been fully reported, and the interaction of the entire $[Ru(bqp)_2]^{2+}$ family with DNA is unknown. Herein, we report the DNA binding properties of **cis**, **trans** and **mer** with B-form double stranded (DS), the G-quadruplex forming sequence from the human telomere (hTeloG),[31] the i-motif found in the promoter region of the death associated protein gene (DAP),[3] and the i-motif forming sequence from the human telomere (hTeloC).[32] We find that of the three $[Ru(bqp)_2]^{2+}$ isomers, one (**cis**) shows a significant light switch effect and, through emission lifetime measurements, is able to indicate the presence of the DAP i-motif, even in a mixture with other types of DNA structures. Separated enantiomers of **cis** also revealed **Λ-cis** to have a preference for i-motif whereas **Δ-cis** prefers double helical DNA. None of the $[Ru(bqp)_2]^{2+}$ isomers have the free hydrogen bonding groups seen in dppz, and DFT and molecular docking calculations suggest that the light-switching effect instead originates from steric compression and electronic effects in a tight binding site. These favor a more compact, emissive ^{3}MLCT state and disfavor a distorted (stretched), non-emissive triplet metal-centered (^{3}MC) state – a previously unreported light switching mechanism.

RESULTS AND DISCUSSION

Firstly, to investigate the strength of $[Ru(bqp)_2]^{2+}$-DNA interactions, electronic absorption titrations were carried out and the intrinsic binding constants (K_b) were calculated using a linear regression model (see Table 1 and Figures S1-3).[33,34] The **cis** isomer (racemate) shows the strongest binding with the majority of DNA secondary structures, with K_bs comparable to other, strongly binding Ru-based light switching complexes ($\times 10^6$ M^{-1}).[23,24] Its strongest binding is to the i-motif DAP and DS, with a 10-fold difference in binding between the i-motif DAP and the G-quadruplex hTeloG. In contrast, **mer** exhibited comparatively lower binding affinities for all types of DNA. These results are consistent with the sizes and shapes of the three isomers. It seems that the facial arrangement of the bqp ligand around the Ru centre improves the interaction with DNA; both **cis** and **trans** have stronger binding with all types of DNA compared to **mer**. The difference between **cis** and **trans** may be explained by the different angle between the central pyridines (92° and 180°, respectively, see Figure 1). This makes **cis** smaller along one axis than either **trans** or **mer**, potentially allowing it to access a tighter space within the structure, especially the i-motif, which is more compact than DS DNA.[1]

Steady-state emission experiments were performed to further assess the effect of DNA on the photophysical properties of the isomers. The **cis** and **trans** isomers in buffer show very little steady-state emission, with **cis** displaying a very large increase in emission upon addition of DNA, depending on the type of structure (Figure 2, Table 1 and Figures S4-6). The greatest "switch on" effect was observed with the **cis** isomer and DS (>50-fold), followed by the i-motif structures DAP and hTeloC. This is in stark contrast to the **mer** isomer, which shows a very intense ^{3}MLCT emission in buffer and either no increase or a small increase in intensity in the presence of DNA. The **trans** isomer does not "switch on" as fully as **cis**, producing a low emission intensity with all types of DNA. Contrary to other light switching complexes,[13] **cis** shows no significant emission enhancement in organic media compared to water (Figure S7). This, together with the absence of hydrogen bonding groups within the structure of complexes, imply a different "switch on" mechanism to dppz complexes.[15] Similarly, aggregation-induced emission (AIE)[35] was also not responsible for the switching mechanism (Figure S8).

A fluorescence indicator displacement (FID) assay with thiazole orange (TO) was also performed to provide another measure of relative binding affinity (see Table S1 and Figure S13-15). This also showed that **cis** displaces TO better than **mer** and **trans** for all types of DNA, and most effectively from the i-motif DAP, further corroborating the other data presented here.

The properties of these complexes with DNA are exciting as the **cis** isomer shows promising i-motif binding. Recent work by Vilar and co-workers has shown how emission lifetime measurements can lead to G-quadruplex identification even where emission intensity studies fail to do so.[36,37] To probe the potential for these complexes to identify i-motif, luminescence lifetimes were acquired using multi-channel scaling (MCS) (Figure 3, Figures S16-18 and Tables S2-3). In the absence of DNA, the **mer** isomer displays a biexponential decay from a ^{3}MLCT excited state, with the second component having a long-lived emission and an amplitude of

>0.90, indicating that this component is responsible for the overall emission of the complex. Upon addition of DNA, this component becomes much longer-lived but less populated, leading to the unremarkable changes seen in the emission intensity studies. The two facial isomers exhibit much shorter decays in the absence of DNA, consistent with their weaker emission intensity, although both still have ^{3}MLCT character. In the presence of DNA, the $\bar{\tau}$ of **trans** increases in line with the trend seen in emission intensity studies, with the second component gaining in lifetime and population. The decay profile of the **cis** isomer is better described as a three-component decay in the presence of DNA. This could either be due to the emergence of a new, previously inaccessible, ^{3}MLCT state or is reflective of a subpopulation of chromophore that is bound and experiences a change in its ^{3}MLCT state. This third component greatly increases the $\bar{\tau}$ of **cis** in the presence of DNA and in the case of DAP, it is almost 10-fold longer. However, the amplitude of this component more closely mirrors the trend in emission intensity increases than its lifetime does. For example, in the case of **cis** and DS, the steady-state intensity increase is larger than that with **cis** and DAP and the amplitude of the third component is greater (0.26 vs 0.21, respectively see Table 2), even though its lifetime is shorter. This implies that it is the population of this state that causes the light switching behavior.

Table 1. Biophysical properties of the isomers with different DNA sequences

		Intrinsic Binding Constant (K_b) [x10^6 M^{-1}][a]	Red Shift in Absorbance [nm][b]	Hypochromicity in Absorbance (%)[b]	Normalised Emission Increase[c]	Estimated Dissociation Constant (K_d) [μM][d]	Number of contacts with DNA[d]
mer	DAP	0.60 ± 0.01	6 ± 2	26 ± 2	1.02 ± 0.04	ND	ND
	DS	0.78 ± 0.13	3 ± 1	27 ± 1	1.03 ± 0.02	1.33	65
	hTeloC	0.63 ± 0.00	4 ± 1	27 ± 2	0.00 ± 0.01	1.80	27
	hTeloG	0.30 ± 0.13	4 ± 0	37 ± 1	0.93 ± 0.43	2.41	42
trans	DAP	3.39 ± 1.40	7 ± 1	18 ± 1	5.42 ± 0.30	ND	ND
	DS	3.33 ± 0.24	8 ± 1	13 ± 5	3.40 ± 0.28	2.22	65
	hTeloC	2.27 ± 0.43	6 ± 1	42 ± 1	2.90 ± 0.71	1.18	34
	hTeloG	2.24 ± 0.73	8 ± 1	25 ± 0	3.26 ± 0.79	0.24	65
cis	DAP	6.94 ± 0.26	7 ± 0	48 ± 2	41.19 ± 0.24		
	DS	8.40 ± 1.01	7 ± 0	21 ± 0	54.67 ± 2.83		
	hTeloC	1.13 ± 0.15	9 ± 1	30 ± 2	21.95 ± 0.10		
	hTeloG	0.63 ± 0.02	7 ± 1	48 ± 0	15.85 ± 0.66		
Λ-cis	DAP	3.13 ± 0.06	6 ± 1	35 ± 3	46.53 ± 2.37	ND	ND
	DS	1.21 ± 0.20	4 ± 1	26 ± 1	21.37 ± 4.97	2.23	69
	hTeloC	2.73 ± 0.76	5 ± 1	33 ± 2	29.18 ± 2.52	0.40	117
	hTeloG	0.57 ± 0.11	1 ± 1	37 ± 3	23.89 ± 1.19	0.20	66
Δ-cis	DAP	3.88 ± 0.60	7 ± 1	30 ± 3	59.76 ± 0.70	ND	ND
	DS	4.62 ± 0.93	7 ± 1	36 ± 3	78.78 ± 2.60	1.69	82
	hTeloC	0.58 ± 0.13	5 ± 1	33 ± 2	28.92 ± 0.07	0.99	93
	hTeloG	0.53 ± 0.20	5 ± 1	37 ± 3	20.09 ± 4.27	0.17	65

Buffers used: 10 mM KCl, 100 mM sodium cacodylate at pH 6.8 (hTeloG, DAP or DS) or pH 5.5 (hTeloC). [a] From electronic absorption titration of 4.5 μM and 0-20 μM DNA using a linear regression model [b] From end point of electronic absorption titration [c] Using 4.5 μM Ru complex and 7.7 μM DNA (λ_{ex} = 490 nm (**mer**), 590 nm (**cis**) and 550 nm (**trans**), λ_{em} = 690 nm (**mer**), 700 nm (**cis** and **trans**)) (see Figure S4-6) [d] From docking the flexible Ru crystal structures to PDB: 1KF1 (hTEloG), 1ELN (hTeloC) and DS (built using Chimera 1.10.2) and minimized using the AMBER ff99bsc0 force field, $K_d = e^{\Delta G/RT}$.

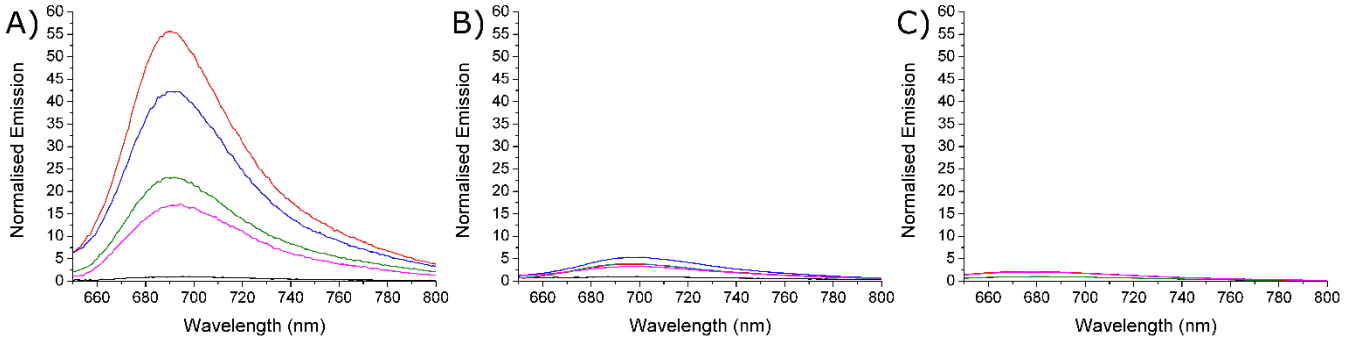

Figure 2 - Normalized emission intensity of 4.5 μM a) **cis**, b) **trans**, and c) **mer** in the absence of DNA (black) and in presence of 7.7 μM hTeloC (green), DAP (blue), DS (red) and hTeloG (pink) in 10 mM sodium cacodylate, 100 mM KCl and pH corrected to 6.8 (hTeloG, DAP or DS) or pH 5.5 (hTeloC)

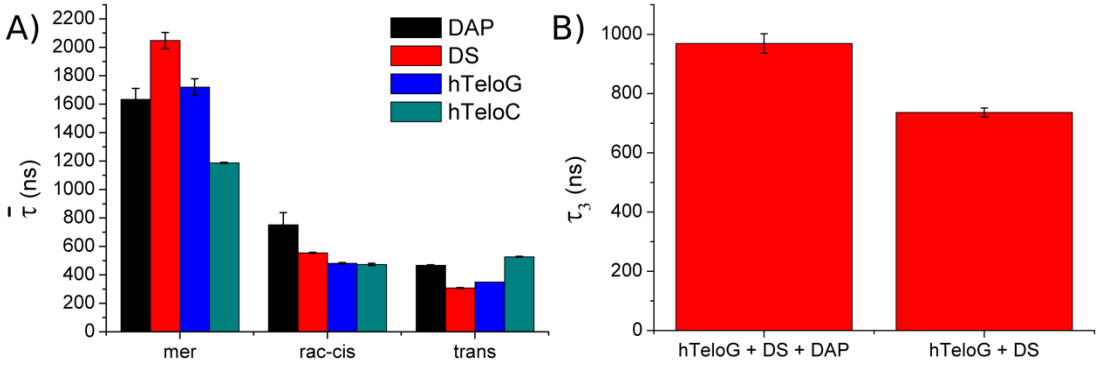

Figure 3 – $\bar{\tau}$ of **A) mer**, *rac*-**cis** and **trans** in the presence of DAP (black), DS (red), hTeloG (blue) and hTeloC (green), and **B)** τ_3 of cis in the presence of hTeloG, DS and DAP (left) and hTeloG and DS (right) (see Table S2)

However, the lifetime increase seen with DAP is greater than that with other types of DNA, with the τ_3 value approximately 300 ns longer. This is a remarkably longer decay lifetime than either the unbound complex or that bound to other DNA types. We questioned whether the increase in τ_3 could be used to identify the DAP i-motif, even in the presence of other DNA types. To test this, the lifetime was measured in a solution that contained a mixture of DS and G-quadruplex DNA, yielding a decay profile almost identical to that of when bound to DS (Figure 3 and Table S2). To a separate solution containing DS, G-quadruplex and DAP, was added **cis**, yielding a larger lifetime (τ_3) increase and a decay profile more reflective of that when bound to DAP (Figures 3, S2 and Table S2). While the third component in this experiment is complex – originating from **cis** bound to DS and hTeloG as well as DAP – at 969 ns it is >200 ns longer than that for **cis**+DS+hTeloG. In no other experiment does it exceed 800 ns except **cis**+DAP alone (1049 ns). Thus, it is indicative of the presence of the DAP i-motif. To our knowledge, this is the first example of a small-molecule with i-motif–detecting capability in the presence of other types of DNA. While the results with hTeloC make it clear that there is still work to do to make a general i-motif probe, this may provide a starting point for development of small molecule (rather than antibody-based) i-motif detection *in vivo*.

Given the interesting properties of the racemic **cis** isomer, we considered the possibility that one of the enantiomers may have a preference for i-motif over double helical DNA (and vice versa). Separation of the **cis** isomers was performed using chiral HPLC to give both **Δ-cis** and **Λ-cis** and their identity confirmed by obtaining a crystal structure of the Δ-enantiomer (Table S4, Figure S20). Their biophysical properties are described in Table 1. Indeed, this revealed that there is a difference in the binding properties of the enantiomers. **Λ-cis** was found to bind i-motif better (3.13×10^6 M^{-1} and 2.73×10^6 M^{-1} for DAP and hTeloC respectively) compared to G-quadruplex (0.57×10^6 M^{-1}) or double helical DNA (1.21×10^6 M^{-1}). In contrast, **Δ-cis** exhibits strongest binding to double helical DNA (4.62×10^6 M^{-1}). Interestingly, the binding properties of the racemic **cis** are not simply an average of the two enantiomers, indicating potentially complicated binding events. Given each enantiomer can potentially change the structure of DNA, and therefore a binding event can change affinity for alternative binding sites, this is not unexpected. Similar to the binding properties, the emission enhancement is also different for each **cis** enantiomer. **Λ-cis** shows the largest increase in emission for DAP, followed by hTeloC, indicating this enantiomer has a preference for i-motif. Similarly, **Δ-cis** shows the largest light-up effect for double helical DNA (Figure 4).

To support the experimental evidence for binding, we used computational docking to investigate the binding strengths and locations of the isomers with i-motif, G-quadruplex and double-stranded DNA. Docking the crystal structures of the three isomers[27,30] using AutoDock 4.2[38] yielded a lower estimated dissociation constant (K_d) for the **Λ-** and **Δ-cis**

Table 2: Amplitude and lifetime of each component obtained from multi-channel scaling (MCS) experiments of 4.5 μM **mer**, **cis**, and **trans** with 20 μM DNA

		α1	τ1 (ns)	α2	τ2 (ns)	α3	τ3 (ns)	avg τ (ns)	Normalised increase of avg τ vs No DNA
Δ-cis	No DNA	0.96 ± 0.02	23 ± 1	0.04 ± 0.02	338 ± 1			37 ± 6	
	DAP	0.38 ± 0.07	24 ± 15	0.43 ± 0.06	187 ± 15	0.18 ± 0.01	802 ± 21	238 ± 23	6.49 ± 0.64
	DS	0.35 ± 0.10	59 ± 15	0.32 ± 0.06	229 ± 79	0.33 ± 0.04	673 ± 29	312 ± 7	8.51 ± 0.18
	hTeloC	0.49 ± 0.03	57 ± 2	0.37 ± 0.02	200 ± 11	0.14 ± 0.01	865 ± 26	222 ± 1	6.07 ± 0.04
	hTeloG	0.50 ± 0.01	19 ± 3	0.37 ± 0.00	121 ± 12	0.13 ± 0.01	621 ± 8	135 ± 12	3.69 ± 0.32
Λ-cis	No DNA	0.97 ± 0.02	23 ± 1	0.03 ± 0.02	340 ± 44			33 ± 4	
	DAP	0.38 ± 0.10	28 ± 14	0.44 ± 0.06	186 ± 25	0.17 ± 0.04	751 ± 26	225 ± 57	6.79 ± 1.71
	DS	0.46 ± 0.09	39 ± 18	0.48 ± 0.08	130 ± 27	0.06 ± 0.00	702 ± 62	121 ± 14	3.64 ± 0.43
	hTeloC	0.35 ± 0.01	45 ± 3	0.50 ± 0.01	162 ± 2	0.14 ± 0.00	702 ± 48	199 ± 11	6.00 ± 0.33
	hTeloG	0.43 ± 0.00	28 ± 2	0.43 ± 0.00	159 ± 3	0.15 ± 0.01	799 ± 14	198 ± 0	5.97 ± 0.00
***rac*-cis**	No DNA	0.96 ± 0.02	23 ± 1	0.04 ± 0.02	338 ± 1			37 ± 6	
	DAP	0.40 ± 0.01	62 ± 14	0.39 ± 0.02	261 ± 14	0.21 ± 0.03	1049 ± 40	352 ± 27	9.61 ± 0.75
	DS	0.43 ± 0.02	62 ± 3	0.32 ± 0.02	181 ± 0	0.26 ± 0	746 ± 17	275 ± 0	7.51 ± 0.00
	hTeloC	0.36 ± 0.10	57 ± 15	0.47 ± 0.09	192 ± 23	0.17 ± 0.01	783 ± 48	239 ± 3	6.53 ± 0.08
	hTeloG	0.45 ± 0.04	37 ± 6	0.41 ± 0.03	177 ± 13	0.14 ± 0.01	757 ± 49	197 ± 4	5.38 ± 0.11
	hTeloG and DS	0.39 ± 0.03	44 ± 5	0.36 ± 0.03	171 ± 13	0.25 ± 0.01	736 ± 15	562 ± 14	
	hTeloG, DS and DAP	0.41 ± 0.02	50 ± 4	0.40 ± 0.02	231 ± 13	0.19 ± 0.01	969 ± 33	679 ± 25	
mer	No DNA	0.07 ± 0.00	166 ± 8	0.93 ± 0.00	768 ± 12			758 ± 11	
	DAP	0.23 ± 0.05	341 ± 29	0.77 ± 0.05	1,714 ± 51			1,634 ± 77	2.15 ± 0.10
	DS	0.15 ± 0.05	191 ± 17	0.85 ± 0.05	2,080 ± 42			2,048 ± 56	1.25 ± 0.03
	hTeloC	0.56 ± 0.07	610 ± 26	0.44 ± 0.07	1,498 ± 81			1,187 ± 4	0.69 ± 0.00
	hTeloG	0.18 ± 0.04	318 ± 95	0.82 ± 0.04	1,764 ± 36			1,720 ± 58	0.84 ± 0.03
trans	No DNA	0.81 ± 0.01	43 ± 2	0.19 ± 0.01	524 ± 25			136 ± 2	
	DAP	0.60 ± 0.01	213 ± 6	0.40 ± 0.01	849 ± 17			468 ± 3	3.44 ± 0.02
	DS	0.71 ± 0.01	176 ± 5	0.29 ± 0.01	628 ± 18			308 ± 3	2.26 ± 0.02
	hTeloC	0.55 ± 0.01	216 ± 7	0.45 ± 0.01	907 ± 17			527 ± 3	3.87 ± 0.02
	hTeloG	0.65 ± 0.01	153 ± 4	0.35 ± 0.01	713 ± 14			350 ± 2	2.57 ± 0.01

isomers with i-motif and G-quadruplex DNA compared to the **trans** and **mer** isomers (see Table 1), indicating stronger binding. The trend is not the same for double helical DNA, where even in the docking studies, it is clear that the **Λ-** and **Δ-cis** isomers have different binding strengths, with **Δ-cis** binding better than **Λ-cis**. In these regards, the molecular docking calculations replicate experimental trends, although they do not accurately replicate the order of binding strength across all DNA/chromophore combinations. Inspection of the computed binding pockets indicates a contrast with the dppz complexes which end-stack G-quadruplex DNA[25] and bind the loops of i-motif structure.[26] Here the bqp complexes bind the major groove of i-motif DNA. Despite the structural differences between them, all of the bqp isomers seemed to bind in the same pocket for each individual DNA structure (Figures S9-11). Both **Λ-** and **Δ-cis** made more DNA-contacts compared to the other isomers, for all types of DNA structures tested, supporting the notion that the smaller size of **cis** allows it to access a tighter space within DNA structures. This is clearest with i-motif DNA, where all isomers bind in the major groove but, by virtue of their different structures, they cannot all access the pocket in the same way. **Δ-cis** has 93 and **Λ-cis** has 117 contacts with the DNA whereas the **mer** and **trans** isomers have only 27 and 34, respectively. For the **Λ-cis** isomer, 68 of these contacts occur with just four cytosine residues in the core of the i-motif, and **Δ-cis** makes fewer contacts, 52, with the same four residues (Figure S12). The **mer** and **trans**

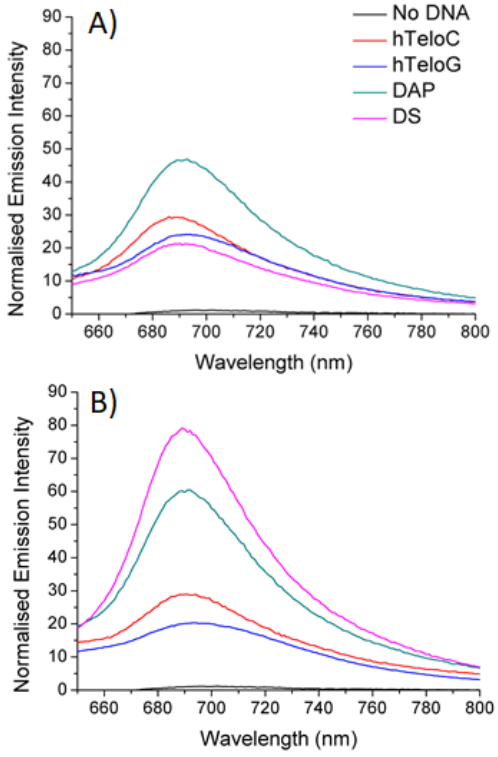

Figure 4 – Normalized emission intensity of 4.5 μM a) **Λ-cis** and b) **Δ-cis** in the absence of DNA (black) and in presence of 7.7 μM hTeloC (green), DAP (blue), DS (red) and hTeloG (pink) in 10 mM sodium cacodylate, 100 mM KCl and pH corrected to 6.8 (hTeloG, DAP or DS) or pH 5.5 (hTeloC)

isomers make even fewer still at 19 and 28, respectively. These interactions demonstrate how the **cis** enantiomers have the potential to bind deeper into the major groove of the i-motif structure. In contrast, the **mer** and **trans** isomers are unable to access the cytosine residues to the same extent, resulting in the larger estimated dissociation constants.

Given the remarkable photophysical properties of the **cis** isomers and evidence indicating a novel "switch on" mechanism, different to dppz complexes, we performed a combined molecular docking/DFT computational study of DNA induced emission switching in **cis**. Ru polypyridyls have an emissive ^{3}MLCT state, and a non-emissive (spectroscopically silent) metal-centered triplet (^{3}MC) that provides the major deactivation pathway.[10,39,40] Prior studies of highly emissive **mer** and much shorter lived (0.25 ns) $[Ru(tpy)_2]^{2+}$ (tpy = terpyridine) indicate three factors that favor ^{3}MLCT for **mer** and thus account for the difference in emission: (i) ^{3}MLCT is *ca.* 0.2 to 0.3 eV lower in energy *vs* ^{3}MC for **mer**, than it is in $[Ru(tpy)_2]^{2+}$,[41-44] (ii) **mer** has a larger transition state barrier for ^{3}MLCT to ^{3}MC conversion (up to 0.25 eV, *vs* 0.08 eV);[43,44] and (iii) **mer**'s triplet potential energy surface has a larger reaction coordinate volume (range of coordination geometries) for ^{3}MLCT, and thus a more entropically favorable emissive state.[43] Moreover, the coordination geometries of ^{3}MC states in general are stretched and cover a large reaction coordinate volume. So, we investigated the hypothesis that DNA exerts an electronic and steric influence on **cis**: encouraging "switch on" by lowering the energy of ^{3}MLCT, and restricting space available for the ^{3}MC. Such a mechanism – based on a shape/size and electronic match – may offer more selectivity than solvent exclusion, and apply to a wide range of other Ru complexes currently considered to be non-emissive.

Calculated ground state (GS) structures of **mer**, **Δ-** and **Λ-cis**, and **trans** (ADF2018, PBE0dDsc/TZP) produced good matches to the X-ray crystal structures (Tables S4 and S5), with the **mer** geometry comparable to the best in the literature.[29,41] Single-point electronic structure calculations (B3LYP/TZP) on these for **mer** (Figure S21), **cis** and **trans** (Figure 5) were also consistent with expectations from the literature, ligand field theory and experimental UV-vis spectra, while TD-DFT computed electronic transitions (Figure S22, Tables S6-S8) showed that as expected, the 600 to 400 nm band is dominated by transitions from Ru-d based HOMO/-1/-2 orbitals, to the closely spaced, ligand based LUMO/+1-3. Compared to **mer**, the lowest metal-based antibonding orbitals of **cis** and **trans** are less destabilized *vs* the HOMO, implying a more energetically favorable ^{3}MC. We quantified this by calculating ^{3}MLCT and ^{3}MC geometries of **cis** and **trans** (Table S9). As seen for **mer**,[41-44] substantial lengthening of Ru-N bonds occurs compared to the GS for the ^{3}MC states, most of all along a N(q)-Ru-N(q) axis (q = quinoline), but ^{3}MLCT geometries are little changed *vs* the GS. For **cis** the relative equilibrium energies of the two states are very similar to those calculated for $[Ru(tpy)_2]^{2+}$ [42,43] - with ^{3}MC 0.26 eV below ^{3}MLCT, while for **trans** ^{3}MC is 0.86 eV below ^{3}MLCT. Including dispersion (B3LYP-D3) lowers the relative energy of the ^{3}MLCT states, to 0.18 eV (**cis**) and 0.73 eV (**trans**) above ^{3}MC. This is consistent with the observed weakly emissive nature of **cis** and **trans** in the absence of DNA. The broad experimental and computational similarity to $[Ru(tpy)_2]^{2+}$ suggests that similar additional factors disfavoring the emissive state – low reaction coordinate volume/low entropy for ^{3}MLCT, and a low TS$^{\#}$ barrier to ^{3}MC formation – apply to these complexes. Moreover, prior work on **mer** found that the smoothest pathway from ^{3}MLCT to ^{3}MC involves stretching Ru-N bonds to quinolines *trans* to one another[43] – this will be facilitated in facial complexes such as **cis** and **trans** as these quinolines are not part of the same ligand.

We tested our switch-on hypothesis by first using Autodock to calculate DNA binding of the **cis** triplet geometries as rigid ligands. While ^{3}MLCT binding sites and dissociation constants are little different from the GS, ^{3}MC binds weaker and in some cases, favors a significantly different site (Table 3). This indicates that the stretched N(q)-Ru-N(q) axis in ^{3}MC results in need for a different (larger) binding pocket. Ru-polypyridyl photophysical timescales are faster than molecular recognition and binding, so this is consistent with steric compression by the tight GS DNA binding site disfavoring ^{3}MC - by restricting reaction coordinate volume (entropy), and increasing the TS$^{\#}$ barrier. Secondly, experimental red-shifts and hyperchromicities imply electronic change to **cis** upon binding, and for **Λ-cis** bound to DS and hTeloC the trend in in Autodock dissociation constants is

consistent with experiment. So, for these combinations we performed single-point calculations in the presence of

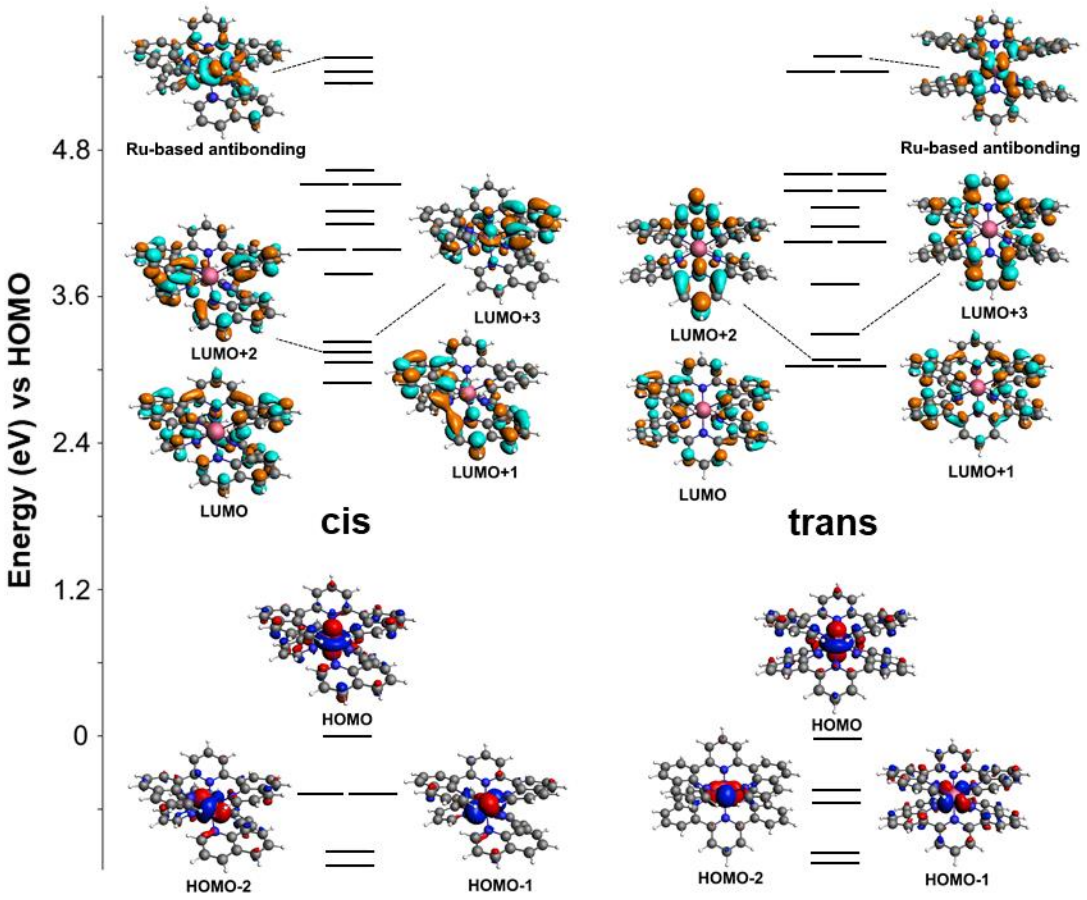

Figure 5 - Electronic structures of **cis** and **trans** with representations of selected orbitals. Calculated in water (SM12 solvation) at the B3LYP/TZP level of theory on PBE0dDsc/TZP geometries.

Table 3. Comparison of the Autodock calculated binding sites of the rigid structures of the GS, ^{3}MLCT and ^{3}MC excited states of **Δ** and **Λ cis**

		GS		**^{3}MLCT**			**^{3}MC**		
		K_d (μM)	DNA contacts	K_d (μM)	DNA con-tacts	Distance from GS (Å)	K_d (μM)	DNA contacts	Distance from GS (Å)
Δ-cis	DS	1.71	64	1.66	63	0.15	4.44	65	0.69
	hTeloC	0.98	66	0.90	66	0.05	2.45	77	0.54
	hTeloG	0.17	65	0.16	67	0.00	0.31	58	4.91
Λ-cis	DS	2.23	60	1.94	65	0.03	4.90	58	3.43
	hTeloC	0.40	79	0.42	80	0.05	2.90	67	0.54
	hTeloG	0.20	66	0.18	65	0.08	0.36	64	4.68

partial charges obtained from the GS DNA binding sites. These positive charges (from the base pairs) tend to have more effect on ligand based orbitals, reducing the HOMO-LUMO gap for Λ-**cis** from 2.903 eV unbound, to 2.309 eV in hTeloC – consistent in sign with the observed red shift. With DS, the change in HOMO-LUMO gap is insignificant, but for both types of DNA ^{3}MLCT becomes more stable upon binding – shifting down by 0.29 eV *vs* ^{3}MC with hTeloC, and 0.04 eV with DS. Although quantitative predictions of emission cannot be made from equilibrium energies, work on Ru tpy analogues has associated a computed 0.11 eV fall in the energy of ^{3}MLCT *vs* ^{3}MC with a 50× increase in experimental excited state lifetime.[45]

Our simple model – steric restriction of coordination geometries, and electronic influence of DNA, is consistent with

experimental data for the separated **cis** enantiomers, and also **trans**, where in almost all cases larger K_bs (indicating tighter binding sites) yield larger absorption red shifts and hyperchromicities (indicating more electronic influence), larger emission intensity increases and larger lifetime increases. For **mer**, there is effectively no change in emission because the ^{3}MLCT state is already strongly favored. Although computationally delineating the steric and electronic contributions is beyond the scope of this study, the experimental results for **trans** provide some insight. In many cases, these imply just as tight a binding pocket and similar electronic effects to those seen with **cis**, yet due to the larger energetic difference between the ^{3}MC and ^{3}MLCT, a much weaker switch on effect occurs. This does not preclude a contribution from steric compression, but it more directly implicates an electronic effect as strong steric compression would likely produce a similar switch on for both **cis** and **trans**.

CONCLUSIONS

In summary, we have shown that the structural arrangement of the bqp ligand around Ru^{2+} alters the biophysical, as well as photophysical, properties of the complex and that the photophysical properties change upon binding to DNA. Electronic absorption, time-resolved emission, TO displacement and computational data all show that **cis** binds most DNA types more effectively than **mer** or **trans**, and the single enantiomer **Λ-cis** shows preference for i-motif through binding and switch-on effect in the presence of i-motif DNA. The fact that even racemic *cis,fac*-$[Ru(bqp)_2]^{2+}$ not only acts as a DNA light switch but also, through emission lifetimes, can indicate the presence of the i-motif from the promoter region of DAP in a mixture other DNA secondary structures, has great implications for the further development of phosphorescent light switching complexes for use as DNA secondary structure probes. The mechanism of the "switch on" effect in these complexes is clearly working via a different mechanism to dppz species. The fact that emission is not driven by solvent exclusion and arises on actual binding to DNA offers advantages regarding specificity against other biological targets (such as proteins, lipids and carbohydrates). Moreover, our work suggests that many previously published non-emissive Ru complexes could switch on in DNA or other biological molecules with suitable binding sites, making them excellent probes. This opens up a plethora of opportunity in this field. Further work, focused on refining understanding of the switching mechanism and developing analogues with enhanced emission properties, will expedite this development.

EXPERIMENTAL

General Methods

Microwave heating was performed using a Biotage Initiator+ microwave synthesizer in a 5 mL sealed microwave vial. HPLC analysis was carried out using an Agilent 1260 infinity with a reverse-phase C18 column. ^{1}H NMR spectra were recorded using a Bruker 400 MHz spectrometer and chemical shifts are reported in parts per million (ppm) relative to the residual solvent. 2,6-bis(8′-quinolinyl)pyridine,[27] $Ru(DMSO)_4Cl_2$[46] and *mer*-, *cis,fac*- and *trans,fac*-$[Ru(2,6\text{-bis}(8'\text{-quinolinyl})pyridine)_2][PF_6]_2$[30] were synthesised following the published literature procedures.

DNA Sequences

Sequences were bought from Eurogentec with RP-HPLC purification and made up to a 1 mM stock solution using MilliQ water. The concentrations were then checked using a nanodrop to read the absorbance at 260 nm and the extinction coefficient supplied from the manufacturer used to calculate the concentration. The sequences used are hTeloC = (5'-d[TAA-CCC-TAA-CCC-TAA-CCC-TAA-CCC]-3'), hTeloG = (5'-d[GGG-TTA-GGG-TTA-GGG-TTA-GGG-TTA]-3'), DS = (5'-d[GGC-ATA-GTG-CGT-GGG-CGT-TAG-C]-3') and its complementary sequence (5'-d[GCT-AAC-GCC-CAC-GCA-CTA-TGC-C]-3'), DAP = (5'd[CCC-CCG-CCC-CCG-CCC-CCG-CCC-CCG-CCC-CC]-3'). All buffers used were 100 mM potassium chloride and 10 mM sodium cacodylate that were pH corrected to pH 5.5 (hTeloC) or pH 6.8 (hTeloG, DS, and DAP). All DNA samples were thermally annealed in a heat block at 95°C for 5 minutes and left overnight to return to room temperature.

mer-$[Ru(2,6\text{-bis}(8'\text{-quinolinyl})pyridine)_2][PF_6][Cl]$ (mer)

A crude mixture of *mer*, *cis,fac* and *trans,fac*-$[Ru(2,6\text{-bis}(8'\text{-quinolinyl})pyridine)_2][PF_6]_2$ (200 mg, 0.189 mmol) was dissolved in acetonitrile and tetrabutylammonium chloride (210 mg, 0.756 mmol) was added and left to stir for 30 min. The red solid was filtered and washed with acetone and the three isomers were then separated by preparative HPLC (40-60% MeOH/H_2O plus 0.1% CF_3CO_2H over 30 min, Figure S23). ^{1}H NMR (400MHz, CD_3OD): δ: 8.13 (t, *J*=8.0 Hz, 2 H), 8.08 (s, 4 H), 8.06 (dd, *J*=4.5, 1.4 Hz, 4 H), 7.91 (d, *J*=8.2 Hz, 4 H), 7.75 (dd, *J*=7.5, 1.1 Hz, 4 H), 7.66 (dd, *J*=8.2, 1.0 Hz, 4 H), 7.42 (t, *J*=7.8 Hz, 4 H), 7.04 ppm (dd, *J*=8.0, 5.3 Hz, 4 H). ^{13}C NMR (101 MHz, CD_3OD) δ: 159.69, 158.31, 148.03, 139.60, 138.95, 134.35, 133.29, 132.06, 129.20, 128.26, 128.12, 123.33. FTMS ($[C_{46}H_{30}N_6Ru]^{2+}$) m/z: calc: 384.0787 found: 384.0785. Anal. Calcd for $C_{46}H_{30}N_6RuClPF_6 \bullet 4H_2O$: C, 54.13; H, 3.76; N, 8.24; found: C, 54.14; H, 3.34; N, 8.50.

cis,fac-$[Ru(2,6\text{-bis}(8'\text{-quinolinyl})pyridine)_2][PF_6][Cl]$ (cis)

The complex was isolated as a fraction from the synthesis of ***mer*** to yield a purple solid. ^{1}H NMR (400MHz, CD_3OD): δ: 8.83 (dd, *J*=5.3, 1.1 Hz, 2 H), 8.78 (dd, *J*=8.2, 0.9 Hz, 2 H), 8.38 (dd, *J*=8.1, 0.9 Hz, 2 H), 8.29 (dd, *J*=7.3, 1.2 Hz, 2 H), 8.24 (dd, *J*=8.2, 1.0 Hz, 2 H), 8.17 (dd, *J*=8.1, 0.9 Hz, 2 H), 7.93 (dd, *J*=8.2, 5.3 Hz, 2 H), 7.89 (dd, *J*=5.4, 1.3 Hz, 2 H), 7.83 (t, *J*=8.0 Hz, 2 H), 7.74 - 7.79 (m, *J*=4.0, 4.0, 3.1 Hz, 4 H), 7.70 (t, *J*=7.8 Hz, 2 H), 7.43 (dd, *J*=7.5, 1.2 Hz, 2 H), 7.31 (dd, *J*=8.1, 1.2 Hz, 2 H), 6.77 ppm (dd, *J*=8.2, 5.3 Hz, 2 H). ^{13}C NMR (101 MHz, CD_3OD) δ: 159.52, 158.88, 138.86, 137.61, 132.32, 132.24, 131.44, 130.59, 130.14, 129.66, 129.18, 127.84, 127.58, 126.90, 125.63, 122.45, 121.67. FTMS ($[C_{46}H_{30}N_6Ru]^{2+}$) m/z: calc: 384.0787 found: 384.0785. Anal. Calcd for $C_{46}H_{30}N_6RuClPF_6 \bullet 4H_2O$: C, 54.13; H, 3.76; N, 8.24; found: C, 53.70; H, 3.93; N, 7.91.

trans,fac-$[Ru(2,6\text{-bis}(8'\text{-quinolinyl})pyridine)_2][PF_6][Cl]$ (trans)

The complex was isolated as a fraction from the synthesis of ***mer*** to yield a purple solid. ^{1}H NMR (400MHz, CD_3OD): δ:

9.19 (dd, *J*= 5.2, 1.3 Hz, 4H), 8.14 (t, *J* = 8.0, 2H), 8.06 (dd, *J* = 8.1, 0.7 Hz, 4 H), 7.86 (dd, *J* = 7.5, 1.1 Hz, 4H), 7.81 (d, *J* = 8.2 Hz, 4H), 7.68 (dd, *J* = 8.0, 0.8 Hz, 4H), 7.47 (m, 8 H). ^{13}C NMR (101 MHz, CD_3OD) δ: 160.64, 160.00, 139.98, 138.76, 138.73, 133.44, 133.36, 132.56, 131.26, 128.96, 128.70, 128.02, 126.75, 123.57, 122.79. FTMS ($[C_{46}H_{30}N_6Ru]^{2+}$) m/z: calc: 384.0787 found: 384.0788. Anal. Calcd for $C_{46}H_{30}N_6RuClPF_6 \bullet 4H_2O$: C, 54.13; H, 3.76; N, 8.24; found: C, 54.11; H, 3.96; N, 8.44.

Separation of Δ- and Λ-cis

Separation was achieved on a Chiralpak IC00CG-MA002 HPLC column with 10% MeOH in EtOH and 0.05% TFA over 30 mins (Figure S24). Multiple runs were performed with a 100 μL injection of a 5 mg mL^{-1} solution of the racemic mixture in MeOH. The fractions were combined and collected for each enantiomer and solvent removed via rotary evaporation. The solids were then dissolved in MeOH and stirred overnight in thoroughly washed Amberlite IRA-400, which was then filtered to remove the resin. After removal of the solvent, the solid was then dissolved in water to form a 10 mM stock solution. The circular dichroic spectra were collected for each enantiomer and the extinction coefficient obtained from their absorbance trace to ensure purity (see Figure S24 and S25). X-ray diffraction quality samples were also obtained of the Δ enantiomer by slow diffusion of diethyl ether into a MeOH solution.

X-ray Crystallography. Crystals of Δ-[***cis***-1][CF_3CO_2]$_2$•1.5MeOH•H_2O were grown by slow diffusion of diethyl ether into a MeOH solution. Data were collected on a Rigaku XtalLab Synergy S diffractometer equipped with a PhotonJet Cu micro-focus source and a Hypix hybrid photon counting detector. Data reduction, cell refinement and absorption collection were carried out using Rigaku CrysAlisPro[47] software and solved using SHELXT-2018[48] *via* Olex2-1.3.[49] Refinement was achieved by full-matrix least-squares on all F_0 data using SHELXL-2018[50] and molecular graphics were prepared using Ortep-3.[51] The structure required application of restraints (SIMU and RIGU) on the thermal parameters of several carbon atoms of the Δ-[***cis***-1]$^{2+}$ unit, in addition to restraints on interatomic distances and the thermal parameters of disordered trifluoroacetate anions. Moreover, the water molecule would not refine successfully with anisotropic thermal parameters, or with H atoms so was refined as an isolated, isotropic O atom with the H added to the overall formula. Full crystallographic data and refinement details are presented in Table S3 and a thermal ellipsoid plot of the asymmetric units in Figure S20.

Emission Intensity

Emission titration experiments were carried out using a Horiba Jobin Yvon Fluorolog spectrofluorometer and an open-top 10 mm quartz cuvette. 4.5 μM of Ru was prepared in the appropriate buffer and spectra obtained using an excitation wavelength of 490 nm (**mer**), 550 nm (**trans**) or 575 nm (**cis**), a 10 nm slit width over a range of 625 – 800 nm (**mer**) or 650 – 800 nm (**cis** and **trans**), an averaging time of 0.1 s, a data interval of 1 nm and a scan rate of 600 nm min^{-1}. DNA was then titrated into the cuvette at intervals between 0 and 20 μM and spectra obtained after each addition. All emission intensity experiments were carried out in triplicate with the error calculated using the standard error and plotted using Origin. The normalised emission increase results were calculated from using the following equation:

$$I_N = I_N = \frac{I}{I_a}$$

where I_N is the normalised emission, I is the emission in the absence of DNA and I_a is the emission at a given DNA concentration.

For the solvent-based experiments, the same procedure was carried out using the parameters above for 4.5 μM **cis**$[PF_6]_2$ in either ethanol, propan-2-ol or acetonitrile.

Absorption Spectroscopy

Absorption spectra were obtained using a JASCO V-730 Spectrometer. The values reported are calculated from the averages of independent repeats, with error reported as the standard error. 4.5 μM Ru solution in the appropriate buffer was made and measured over 310-650 nm, a data interval of 0.5 nm, bandwidth of 1 nm and a scan speed of 400 nm min^{-1}. Varying amounts of DNA were added (up to 20 μM) to this solution at RT and absorption spectra were taken after each addition until no further change was observed. The data was then fitted to a modified linear regression model:[33,34]

$$[DNA] / (\varepsilon_a-\varepsilon_f) = [DNA] / (\varepsilon_b-\varepsilon_f) + 1 / (\varepsilon_a-\varepsilon_f)K_b$$

where [DNA] is the molar concentration of DNA, ε_a, ε_f and ε_b are the extinction coefficients of a given concentration (A_{abs}/[Ru]), the extinction coefficient of the free metal complex and the extinction coefficient of the bound complex, respectively. In a plot of $[DNA]/(\varepsilon_a - \varepsilon_f)$ as a function of [DNA], K_b is given as the ratio of the slope to the intercept.[33] Hypochromicity (H%) was calculated using the following equation:

$$H\% = 100 * (\varepsilon_f - \varepsilon_b) / \varepsilon_f$$

Multi-Channel Scaling (MCS) Phosphorescence Lifetimes

A 4.5 μM Ru solution in the appropriate buffer was made and the lifetime was obtained using an Edinburgh Instruments FS5 with a 485 nm LED source. To this solution was added 20 μM DNA and the lifetime measured again. All decays were recorded until at least 10,000 counts at an emission wavelength of 690 ± 15 nm (**mer**) or 700 ± 15 nm (**cis** or **trans**). Traces were fitted with an exponential tail fitting equation of two components:

$$I(t) = \alpha_1 e^{-t/\tau 1} + \alpha_2 e^{-t/\tau 2} (+ \alpha_3 e^{-t/\tau 3})$$

where $\Sigma\alpha$ is normalised to unity. All traces were fitted with a χ^2 value of between 0.90 and 1.30. All traces were processed using the Fluoracle software package. The values reported are calculated from the averages of independent repeats, with error reported as the standard error.

Fluorescence Intercalator Displacement (FID)

The FID assay was carried out on a BMG CLARIOstar plate reader using an excitation of 430 nm and emission was measured from 450 to 650 nm with the emission at 450 nm

being normalised to 0%. 96-well plates (Corning 96 well solid black flat bottom plates) were used for this assay. 90 μL of thiazole orange (TO) at a concentration of 2 μL in 10 mM sodium cacodylate and 100 mM potassium chloride that was pH corrected to pH 5.5 (hTeloC) or pH 6.8 (DAP, hTeloG and DS) was added to each well. The fluorescence was then measured at 450 nm with an excitation of 430 nm and normalised to 0%. DNA was added to a 1 μM concentration, shaken at 700 rpm in the plate reader for 30s and left to equilibrate for 20 min. After equilibration the fluorescence was measured again and normalised to 100%. After that, additions in to each well (in triplicate) of 0.45 μM Ru complex was added over a range of 0.45 – 4.05 μM. The fluorescence was measured after each addition and normalised between the 0 and 100% levels previously determined. The percentage displacement of TO value (D_{TO}) was calculated from the displacement of TO after the addition of 4.05 μM of Ru complex. The concentration at which 50% of the TO was displaced (DC_{50}) was calculated using Origin software to plot the percentage TO displacement which were then fitted with a dose-response curve and the DC_{50} obtained from solving the equation for y = 50%.

Emission Polarisation Measurements

Experiments were performed on an Edinburgh Instruments FS5. A 4.5 μM solution of Ru was taken and its emission polarization was measured with the emission polarizer at both 0 and then 90°. To this, a known concentration of DNA was added, and the emission polarization was measured again, repeating from 1-20 μM DNA. The polarization was calculated using the following equation:

$$P = (I_{\parallel} - I_{\perp}) / (I_{\parallel} + I_{\perp})$$

where, $I_{\parallel}$ and $I_{\perp}$ are the emission intensity parallel and perpendicular to the excitation plane, respectively (Figure S27).

Aggregation-induced Emission (AIE)

When well dissolved, AIE probes have no or limited emission, but can emit strongly when aggregated, due to the addition of a poorly solubilising solvent, for example.[35] 200 μL mixtures of acetonitrile in water (0% - 90% water) and PEG-300 in water (0% PEG-300 to 90% PEG-300) were made up. For each fraction, two samples were made, one containing 2 μL **cis** (from a 1 mM stock of **cis**$[PF_6]_2$ or **cis**$[PF_6][Cl]$) and one containing 2 μL acetonitrile or water. The sample without **cis** was scanned using an excitation wavelength of 575 nm (**cis**), a 10 nm slit width over a range of 650 – 800 nm (**cis** and **trans**), an averaging time of 0.1 s, a data interval of 1 nm and a scan rate of 600 nm min^{-1} and then subtracted from the samples containing **cis**. The solvent based experiments were conducted similarly to the above experiments using a 10 μM solution of **cis**$[PF_6]_2$ in acetonitrile. All data were plotted using Origin.

Computational Docking

Docking simulations were carried out with AutoDock 4.2 > and either the telomeric i-motif (PDB: 1ELN),[52] the telomeric G-quadruplex stabilised by K^+ (PDB: 1KF1)[53] or the same double-stranded DNA sequence as that used experimentally in this paper (GGC-ATA-GTG-CGT-GGG-CGT-TAG-C) and its complementary sequence built using Chimera 1.10.2 and minimized using the AMBER ff99bsc0 force field. Ground state structures of the three ruthenium complexes were obtained from their previously published crystal structures,[27,30] triplet excited states were computed via DFT. Ligands and receptors were prepared using the provided python scripts in the MGLTools package and docking was accomplished using a Lamarckian Genetic Algorithm. This was done allowing flexibility in the Ru complexes for the binding study, but for the combination with DFT rigid Ru complexes were used to ensure different excited state geometries were preserved. Ruthenium atom parameters used for AutoDock 4.2 were "atom_par Ru 2.96 0.056 12.000 -0.00110 0.0 0.0 0 -1 -1 1 # Non H-bonding". Contacts between Ru complexes and DNA were calculated using Chimera 1.10.2[54] with a Van der Waals overlap of -0.4 Å. The estimated dissociation constant (K_d) was calculated from the estimated free energy of binding (ΔG) obtained from the AutoDock 4.2 calculations using $K_d = e^{\Delta G/RT}$.

DFT calculations. DFT calculations were carried out using the ADF suite.[55-57] All calculations were carried out using the ADF triple-ζ TZP basis set with the zero-order regular approximation (ZORA) to account for relativitstic effects.[58] The dispersion corrected hybrid functional PBE0-dDsc[59,60] was used for all geometry optimisations, as this was found to give the closest match to ground state geometries (also tested were the dispersion corrected hybrid B3LYP-D3[61,62] and the range separated hybrid ωB97X[63]). Other recent work[29,41] has also found inclusion of dispersion important for obtaining correct geometries for bqp complexes. Geometries of triplet states were calculated using unrestricted DFT (uDFT), starting from the ground state geometry for ^{3}MLCT, and from a geometry stretched along an N(quinoline)-Ru-N(quinoline) axis for ^{3}MC. uDFT was used rather than TD-DFT because it is considered to perform better for charge-separated states, such as MLCT states.[42] For single-point calculations of electronic structure and energy the B3LYP[61] functional was used, as this best reproduced experimentally measured electronic absorption spectra (by TD-DFT). To estimate the electronic influence of DNA, single-point calculations for selected isomer/sequence combinations were carried out in the presence of partial charges extracted from AutoDock calculated DNA binding sites. Solvent (water) was introduced using COSMO[64-66] with Allinger atomic radii in geometry optimisations and TD-DFT calculations of electronic spectra. In single-point energy calculations solvent was introduced using SM12[67,68] instead, as COSMO is incompatible with application of the external electric field used to model the electronic effect of DNA.

ASSOCIATED CONTENT

Supporting Information

The Supporting Information is available free of charge on the ACS Publications website.

Experimental methods and supporting Figures S1 – S27 and Tables S1-S9 (pdf)

AUTHOR INFORMATION

Corresponding Author

Tel: +44 (0)1603 59 1972, email: *z.waller@uea.ac.uk; Tel: +44 (0)1603 59 3137, email: *john.fielden@uea.ac.uk

Notes

The authors declare no competing financial interests.

ACKNOWLEDGMENT

This work was supported by the BBSRC Norwich Research Park Biosciences Doctoral Training Partnership, grant number BB/M011216/1 and an EPSRC Capital Award in Support of ECR (EP/S017909/1). We thank Dr. Kevin Vincent of the University of East Anglia (UEA) for acquiring X-ray diffraction data on **Δ-cis**, and Dr. Garth Jones of UEA for helpful discussions on calculations.

REFERENCES

(1) Gehring, K.; Leroy, J-L; Guéron, M. A tetrameric DNA structure with protonated cytosine-cytosine base pairs. *Nature*. **1993,** *363*, 561-565.

(2) Day, H. A.; Pavlou, P.; Waller, Z. A. E. i-Motif DNA: Structure, Stability and Targeting with Ligands. *Bioorg. Med. Chem.* **2014**, *22* (16), 4407–4418.

(3) Wright, E. P.; Huppert, J. L.; Waller, Z. A. E. Identification of Multiple Genomic DNA Sequences Which Form i-Motif Structures at Neutral pH. *Nucleic Acids Res.* **2017**, *45* (6), 2951–2959

(4) Kang, H.; Kendrick, S.; Hecht, S. M.; Hurley, L. H. The Transcriptional Complex Between the BCL2 I-Motif and HnRNP LL Is a Molecular Switch for Control of Gene Expression That Can Be Modulated by Small Molecules. *J. Am. Chem. Soc.* **2014**, *136* (11), 4172–4185.

(5) Kaiser, C.E.; Van Ert, N.A.; Agrawal, P; Chawla, R.; Yang, D.; Hurley, L. H. Insight into the Complexity of the i-Motif and G-Quadruplex DNA Structures Formed in the KRAS Promoter and Subsequent Drug-Induced Gene Repression. *J. Am. Chem. Soc.* **2017**, *139* (25), 8522-8536.

(6) Zeraati, M.; Langley, D. B.; Schofield, P.; Moye, A. L.; Rouet, R.; Hughes, W. E.; Bryan, T. M.; Dinger, M. E.; Christ, D. I-Motif DNA Structures Are Formed in the Nuclei of Human Cells. *Nat. Chem.* **2018**, *10* (6), 631–637.

(7) Biffi, G.; Tannahill, D.; McCafferty, J.; Balasubramanian, S. Quantitative Visualization of DNA G-Quadruplex Structures in Human Cells. *Nat. Chem.* **2013**, *5* (3), 182–186.

(8) Gill, M. R.; Garcia-Lara, J.; Foster, S. J.; Smythe, C.; Battaglia, G.; Thomas, J. A. A Ruthenium(II) Polypyridyl Complex for Direct Imaging of DNA Structure in Living Cells. *Nat. Chem.* **2009**, *1* (8), 662–667.

(9) Kumar, C. V; Barton, J. K.; Turro, N. J. Photophysics of Ruthenium Complexes Bound to Double Helical DNA. *J. Am. Chem. Soc.* **1985**, *107* (19), 5518–5523.

(10) Medlycott, E. A.; Hanan, G. S. Designing Tridentate Ligands for Ruthenium(II) Complexes with Prolonged Room Temperature Luminescence Lifetimes. *Chem. Soc. Rev.* **2005**, *34* (2), 133.

(11) Puckett, C. A.; Barton, J. K. Mechanism of Cellular Uptake of a Ruthenium Polypyridyl Complex. *Biochemistry* **2008**, *47* (45), 11711–11716.

(12) Puckett, C. A.; Barton, J. K. Methods to Explore Cellular Uptake of Ruthenium Complexes. *J. Am. Chem. Soc.* **2007**, *129* (1), 46–47.

(13) Friedman, A. E.; Chambron, J. C.; Sauvage, J. P.; Turro, N. J.; Barton, J. K. A Molecular Light Switch for DNA: Ru(Bpy)2(Dppz)2+. *J. Am. Chem. Soc.* **1990**, *112* (12), 4960–4962.

(14) Li, G.; Sun, L.; Ji, L.; Chao, H. Ruthenium(Ii) Complexes with Dppz: From Molecular Photoswitch to Biological Applications. *Dalton Trans.* **2016**, *45* (34), 13261–13276.

(15) Olson, E. J. C.; Hu, D.; Hörmann, A.; Jonkman, A. M.; Arkin, M. R.; Stemp, E. D. A.; Barton, J. K.; Barbara, P. F. First Observation of the Key Intermediate in the "light-Switch" Mechanism of [Ru(Phen)2dppz]2+. *J. Am. Chem. Soc.* **1997**, *119* (47), 11458–11467.

(16) Liu, X.-W.; Xiao, Y.; Peng, W.-G.; Zhao, L.-J.; Shen, Y.-M.; Zhang, S.-B.; Lu, J.-L. New Designed DNA Light Switch Ruthenium Complexes as DNA Photocleavers and Topoisomerase I Inhibitors. *Appl. Organomet. Chem.* **2018**, *32* (4), e4231.

(17) Mallepally, R. R.; Putta, V. R.; Chintakuntla, N.; Vuradi, R. K.; Kotha, L. R.; Sirasani, S. DNA Binding Behavior, Sensor Studies, Antimicrobial, Photocleavage and In Vitro Cytotoxicity of Synthesized Ru(II) Complexes with Assorted Intercalating Polypyridyl Ligands. *J. Fluoresc.* **2016**, *26* (3), 1101–1113.

(18) Mardanya, S.; Karmakar, S.; Maity, D.; Baitalik, S. Ruthenium(II) and Osmium(II) Mixed Chelates Based on Pyrenyl–Pyridylimidazole and 2,2′-Bipyridine Ligands as Efficient DNA Intercalators and Anion Sensors. *Inorg. Chem.* **2015**, *54* (2), 513–526.

(19) Perdisatt, L.; Moqadasi, S.; O'Neill, L.; Hessman, G.; Ghion, A.; Warraich, M. Q. M.; Casey, A.; O'Connor, C. Synthesis, Characterisation and DNA Intercalation Studies of Regioisomers of Ruthenium (II) Polypyridyl Complexes. *J. Inorg. Biochem.* **2018**, *182*, 71–82.

(20) Boynton, A. N.; Marcélis, L.; McConnell, A. J.; Barton, J. K. A Ruthenium(II) Complex as a Luminescent Probe for DNA Mismatches and Abasic Sites. *Inorg. Chem.* **2017**, *56* (14), 8381–8389.

(21) Rajput, C.; Rutkaite, R.; Swanson, L.; Haq, I.; Thomas, J. A. Dinuclear Monointercalating RuII Complexes That Display High Affinity Binding to Duplex and Quadruplex DNA. *Chem. Eur. J.* **2006,** *12,* (17) 4611-4619.

(22) Baggaley , E.; Gill, M. R.; Green, N. H.; Turton, D.; Sazanovich, I. V.; Botchway, S. W.; Smythe, C.; Haycock, J. W.; Weinstein, J. A.; Thomas, J. A. Dinuclear Ruthenium(II) Complexes as Two-Photon, Time-Resolved Emission Microscopy Probes for Cellular DNA. *Angew. Chemie. Int. Ed.* **2014**, *53* (13), 3367-3371.

(23) Shi, S.; Zhao, J.; Geng, X.; Yao, T.; Huang, H.; Liu, T.; Zheng, L.; Li, Z.; Yang, D.; Ji, L. Molecular "Light Switch" for G-Quadruplexes and i-Motif of Human Telomeric DNA: [Ru(Phen)2(Dppz)]2+. *Dalton Trans.* **2010**, *39* (10), 2490.

(24) Shi, S.; Geng, X.; Zhao, J.; Yao, T.; Wang, C.; Yang, D.; Zheng, L.; Ji, L. Interaction of [Ru(Bpy)2(Dppz)]2+ with Human Telomeric DNA: Preferential Binding to G-Quadruplexes over i-Motif. *Biochimie* **2010**, *92* (4), 370–377.

(25) Haider, S.M.; Neidle, S.; and Parkinson, G. N. A structural analysis of G-quadruplex/ligand interactions. *Biochimie*, **2011,** *93*, 1239–1251.

(26) Pages, B.P.; Gurung, S. P.; McQuaid, K.; Hall, J.P; Cardin, C. J. and Brazier, J. A. Stabilization of Long-Looped i-Motif DNA by Polypyridyl Ruthenium Complexes. *Front. Chem.,* 2019, **7**, 744.

(27) Abrahamsson, M.; Jäger, M.; Österman, T.; Eriksson, L.; Persson, P.; Becker, H. C.; Johansson, O.; Hammarström, L. A 3.0 Ms Room Temperature Excited State Lifetime of a Bistridentate RuII-Polypyridine Complex for Rod-like Molecular Arrays. *J. Am. Chem. Soc.* **2006**, *128* (39), 12616–12617.

(28) Abrahamsson, M.; Becker, H.-C.; Hammarström, L. Microsecond 3 MLCT Excited State Lifetimes in Bis-Tridentate Ru(Ii)-Complexes: Significant Reductions of Non-Radiative Rate Constants. *Dalton Trans.* **2017**, *46* (39), 13314–13321.

(29) Schlotthauer, T.; Suchland, B.; Görls, H.; Parada, G. A.; Hammarström, L.; Schubert, U. S.; Jäger, M. Aryl-Decorated RuII Polypyridyl-Type Photosensitizer Approaching NIR Emission with Microsecond Excited State Lifetimes. *Inorg. Chem.* **2016**, *55* (11), 5405–5416.

(30) Jäger, M.; Kumar, R. J.; Görls, H.; Bergquist, J.; Johansson, O. Facile Synthesis of Bistridentate Ru II Complexes Based on 2,6-Di(Quinolin-8-Yl)Pyridyl Ligands: Sensitizers with Microsecond 3MLCT Excited State Lifetimes. *Inorg. Chem.* **2009**, *48* (7), 3228–3238.

(31) Henderson, E.; Hardin, C. C.; Walk, S. K.; Tinoco, I.; Blackburn, E. H. Telomeric DNA Oligonucleotides Form Novel Intramolecular Structures Containing Guanine·guanine Base

Pairs. *Cell* **1987**, *51* (6), 899–908.
(32) Leroy, J.-L.; Guéron, M.; Mergny, J.-L.; Hélène, C. Intramolecular Folding of a Fragment of the Cytosine-Rich Strand of Telomeric DNA into an i-Motif. *Nucleic Acids Res.* **1994**, *22* (9), 1600–1606.
(33) Wang, L.; Wu, Y.; Chen, T.; Wei, C. The Interactions of Phenanthroline Compounds with DNAs: Preferential Binding to Telomeric Quadruplex over Duplex. *Int. J. Biol. Macromol.* **2013**, *52*, 1–8.
(34) Wolfe, A.; Shimer, G. H.; Meehan, T. Polycyclic Aromatic Hydrocarbons Physically Intercalate into Duplex Regions of Denatured DNA. *Biochemistry* **1987**, *26* (20), 6392–6396.
(35) Sheet, S. K.; Sen, B.; Patra, S. K.; Rabha, M.; Aguan, K.; Khatua, S. Aggregation-Induced Emission-Active Ruthenium(II) Complex of 4,7-Dichloro Phenanthroline for Selective Luminescent Detection and Ribosomal RNA Imaging. *ACS Appl. Mater. Interfaces* **2018**, *10* (17), 14356–14366.
(36) Shivalingam, A.; Izquierdo, M. A.; Marois, A. Le; Vyšniauskas, A.; Suhling, K.; Kuimova, M. K.; Vilar, R. The Interactions between a Small Molecule and G-Quadruplexes Are Visualized by Fluorescence Lifetime Imaging Microscopy. *Nat. Commun.* **2015**, *6* (1), 8178.
(37) Shivalingam, A.; Vyšniauskas, A.; Albrecht, T.; White, A. J. P.; Kuimova, M. K.; Vilar, R. Trianguleniums as Optical Probes for G-Quadruplexes: A Photophysical, Electrochemical, and Computational Study. *Chem. - A Eur. J.* **2016**, *22* (12), 4129–4139.
(38) Morris, G. M.; Huey, R.; Lindstrom, W.; Sanner, M. F.; Belew,R. K.; Goodsell, D. S.; Olson, A. J. AutoDock4 and AutoDockTools4: Automated Docking with Selective Receptor Flexibility. *J. Comput. Chem.* **2009**, *30* (16), 2785–2791.
(39) Winkler, J. R.; Netzel, T. L.; Creutz, C.; Sutin, N. Direct observation of metal-to-ligand charge transfer (MLCT) excited states of pentammineruthenium(II) complexes. *J. Am. Chem. Soc.* **1987**, *109*, 2831.
(40) Calvert, J. M.; Caspar, J. V.; Binstead, R. A.; Westmoreland, T. D.; Meyer, T. J. Metallopolymer photochemistry. Photophysical, photochemical, and photoelectrochemical properties of $(bpy)_2Ru^{II}$< sites bound to poly(4-vinylpyridine). *J. Am. Chem. Soc.* **1982**, *104*, 6620.
(41) Jäger, M.; Freitag, L.; González, L. Using computational chemistry to design Ru photosensitizers with directional charge transfer. *Coord. Chem. Rev.* **2015**, *304-305*, 146.
(42) Borg, O. A.; Godinho, S. S. M. C.; Lundqvist, M. J.; Lunell, S.; Persson, P. Computational Study of the Lowest Triplet State of Ruthenium Polypyridyl Complexes Used in Artificial Photosynthesis. *J. Phys. Chem. A* **2008**, *112*, 4470.
(43) Österman, T.; Abrahamsson, M.; Becker, H.-C.; Hammarström, L.; Persson, P. Influence of triplet state multidimensionality on excited state lifetimes of bis-tridentate Ru^{II} *J. Phys. Chem. A* **2012**, *116*, 1041.
(44) Österman, T.; Persson, P. Excited state potential energy surfaces of bistridentate Ru^{II} complexes – A TD-DFT study. *Chem. Phys*. **2012**, *407*, 76
(45) Abrahamsson, M.; Lundqvist, M. J.; Wolpher, H.; Johansson, O.; Eriksson, L.; Berquist, J. Rasmussen, T.; Becker, H.-C.; Hammarström, L. Norrby, P.-O.; Åkermark, B.; Persson, P. Steric influence on the excited-state lifetimes of ruthenium complexes with bipyridyl-alkanylene-pyridyl ligands. *Inorg. Chem.* **2008**, *47*, 3540.
(46) Evans, I. P.; Spencer, A.; Wilkinson, G. Dichlorotetrakis(Dimethyl Sulphoxide)Ruthenium(II) and Its Use as a Source Material for Some New Ruthenium(II) Complexes. *J. Chem. Soc. Dalton Trans.* **1973**, *0* (2), 204.
(47) *CrysAlisPro* (Version 1.171.40.68a), Rigaku Corporation; Tokyo: Japan, **2019**
(48) Sheldrick, G. M. *SHELXT-2018*, Programs for Crystal Structure Analysis (Release 2018-2); University of Göttingen: Göttingen, Germany, **2018**.
(49) Dolomanov, O. V.; Bourhis, L. J., Gildea, R. J.; Howard, J. A. K. OLEX2: A complete structure solution, refinement and analysis program; Puschmann, H. J. Appl. Cryst. **2009**, *42*, 339.
(50) Sheldrick, G. M. *SHELXL-2018*, Programs for Crystal Structure Analysis (Release 2018-3); University of Göttingen: Göttingen, Germany, **2015**.
(51) Farrugia, L. J. *ORTEP*-3 for Windows – a version of *ORTEP*-III with a Graphical User Interface (GUI) *J. Appl. Cryst.* **1997**, *30*, 565.
(52) Phan, A. T.; Guéron, M.; Leroy, J.-L. The Solution Structure and Internal Motions of a Fragment of the Cytidine-Rich Strand of the Human Telomere. *J. Mol. Biol.* **2000**, *299* (1), 123–144.
(53) Parkinson, G. N.; Lee, M. P. H.; Neidle, S. Crystal Structure of Parallel Quadruplexes from Human Telomeric DNA. *Nature* **2002**, *417* (6891), 376–880.
(54) Pettersen, E. F.; Goddard, T. D.; Huang, C. C.; Couch, G. S.; Greenblatt, D. M.; Meng, E. C.; Ferrin, T. E. UCSF Chimera - A Visualization System for Exploratory Research and Analysis. *J. Comput. Chem.* **2004**, *25* (13), 1605–1612.
(55) te Velde, G.; Bickelhaupt, F. M.; Baerends, E. J.; Fonseca Guerra, C.; van Gisbergen, S. J. A.; Snijders, J. G.; Ziegler, T. Chemistry with ADF. *J. Comput. Chem.* **2001**, *22*, 931.
(56) Fonseca Guerra, C.; Snijders, J. G.; Te Velde, G.; Baerends, E. Towards an order-N DFT method. *J. Theor. Chem. Acc.* **1998**, *99*, 391.
(57) ADF2018.3, SCM, Theoretical Chemistry, Vrije Universiteit, Amsterdam, The Netherlands, **2018**, http://www.scm.com.
(58) van Lenthe, E.; Baerends, E. J.; Snijders, J. G. Relativistic regular two-component Hamiltonians. *J. Chem. Phys.* **1993**, *99*, 4597.
(59) Adamo, C.; Barone, V. Toward reliable density functional methods without adjustable parameters: The PBE0 model. *J. Chem. Phys.* **1999**, *110*, 6158.
(60) Steinmann, S. N.; Corminboeuf, C. Comprehensive Benchmarking of a Density-Dependent Dispersion Correction. *J. Chem. Theory Comput.* **2011**, *59*, 5936.
(61) Stephens, P. J.; Devlin, F. J.; Chabalowski, C. F.; Frisch, M. J. Ab initio calculation of vibrational absorption and circular dichroism spectra using density functional force fields. *J. Phys. Chem.* **1994**, *98*, 11623.
(62) Grimme, S; Ehrlich, S.; Goerigk, L. Effect of the damping function in dispersion corrected density functional theory. *J. Comput. Chem.* **2011**, *32*, 1457.
(63) Chai, J.-D.; Head-Gordon, M. Systematic optimization of long-range corrected hybrid density functionals. *J. Chem. Phys.* **2008**, *128*, 084106.
(64) Klamt, A.; Schüürmann, G. COSMO: a new approach to dielectric screening in solvents with explicit expressions for the screening energy and its gradient. *J. Chem. Soc.*: *Perkin Trans*. **1993**, 799.
(65) Klamt, A. Conductor-like screening model for real solvents: A new approach to the quantitative calculation of solvation phenomena. *J. Phys. Chem.* **1995**, *99*, 2224
(66) Klamt, A.; Jones, V. Treatment of the outlying charge in continuum solvation models. *J. Chem. Phys.* **1996**, *105*, 9972.
(67) Marenich, A. V.; Cramer, C. J.; Truhlar, D. G. Generalized Born solvation model SM12, *J. Chem. Theory. Comput.* **2013**, *9*, 609.
(68) Peeples, C. A.; Schreckenbach, G. Implementation of the SM12 solvation model into ADF and comparison with COSMO. *J. Chem. Theory. Comput.* **2016**, *12,* 4033.

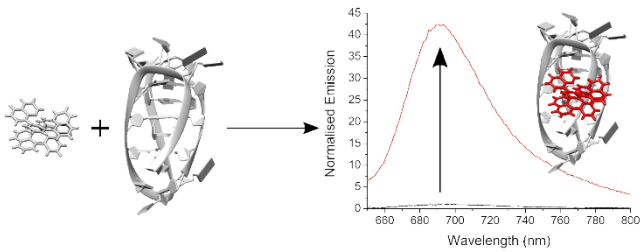
Normalised Emission
45
40
35
30
25
20
15
10
5
0
660
680
700
720
740
760
780
800
Wavelength (nm)